Supporting Information for Characterisation and Modelling of Heterogeneous Sandstone and Carbonate Rocks

DOI: 2021WR029831

Nele Wenck[1], Samuel J. Jackson[2,1], Ann Muggeridge[1],and Samuel Krevor[1]

[1]Department of Earth Science and Engineering, Imperial College London, United Kingdom

[2]CSIRO Energy, Private Bag 10, Clayton South, Victoria 3169, Australia

Contents of this file

Corresponding author: N. Wenck, Department of Earth Science and Engineering, Imperial College London, Exhibition Rd, South Kensington, London SW7 2BU, United Kingdom (nele.wenck15@imperial.ac.uk)

1. Coarsening of the CT Images

Figure S1 assesses the impact of repeat scans and image coarsening on the resultant experimental saturation uncertainty in the saturations for the carbonate samples. The uncertainty was obtained following from the analysis presented in Pini, Krevor, and Benson (2012). As shown, the voxel scale uncertainties are significantly reduced from image coarsening and averaging over repeated scans.

2. 3D Saturation Maps

To evaluate the success of the optimisation workflow, voxel-scale fluid saturations of the experiment and the simulation were compared. Figure S2 to S4 present 3D saturation maps for the three carbonate samples at distinct fractional flows.

3. Modified Modelling Approach: Error Minimisation

Figure S5 demonstrates the results of the history match when including the low and high rate experimental observations as additional fitting targets as applied to the Indiana limestone. The workflow was unable to find a combination of Chierci parameters that minimised the errors in both, the low and high rate observations. As displayed, the smallest error in k_{rw} is achieved at low B values for the low rate experiment (S5a) and at high B values for the high rate experiment (S5c). This disagreement is visible for the other parameters as well. This issue was also encountered for the other two carbonate samples.

4. Impact of the End Effect

The impact of the end effect on the observed rate dependency might have influenced the results. As presented in Jackson, Agada, Reynolds, and Krevor (2018), once end effects are reduced in the digital cores, the severity of rate dependency in the sandstones significantly reduces, more for the Bentheimer than for the Bunter. This showed that it is not just the capillary heterogeneity but also the end effect that is causing the apparent rate dependence. To investigate this for the carbonates, we decided not to shorten the digital cores as was done for the sandstones in Jackson et al. (2018). This is because the heterogeneous feature, specifically for the Edwards Brown, is located close to the outlet. Therefore, shortening the core will remove it. Instead, we set P_c to a finite, but constant value in the end slice, which should also reduce the end effect. Interestingly, the resultant relative permeabilities were unchanged relative to the original results, which indicate that the simulations are not strongly impacted by end effects caused by boundary conditions. This can be explained by the size and orientation of the heterogeneities compared with those in the sandstones. The Bunter sandstone displayed a minimal change in rate dependency after the core was shortened: the perpendicular layers in the Bunter act to compartmentalise the core, meaning that the impact of boundary effects on the core are localised to the few end slices. In comparison to this, the impact of the end effect prevails all the way through the core in the Bentheimer sandstone with a parallel heterogeneity. Therefore, digitally reducing the end effect significantly altered the relative permeability curves. In the carbonates, the vug-matrix systems could act as to compartmentalise the core similar to the Bunter sandstone.

5. Rate Dependency Analysis

Using the iteratively calibrated models for the Bentheimer sandstone, Bunter sandstone and Edwards Brown dolomite, simulations were run at varying flow rates to investigate the rate dependency of relative permeability in detail (Section 3.4 in the main text). The relative permeabilities obtained from these simulations are presented in Tables S1 to S3 at three distinct flow rates.

References

Jackson, S. J., Agada, S., Reynolds, C. A., & Krevor, S. (2018). Characterizing Drainage Multiphase Flow in Heterogeneous Sandstones. *Water Resources Research*, *54*(4), 3139–3161. doi: 10.1029/2017WR022282

Pini, R., Krevor, S. C., & Benson, S. M. (2012). Capillary pressure and heterogeneity for the CO 2/water system in sandstone rocks at reservoir conditions. *Advances in Water Resources*, *38*, 48–59.

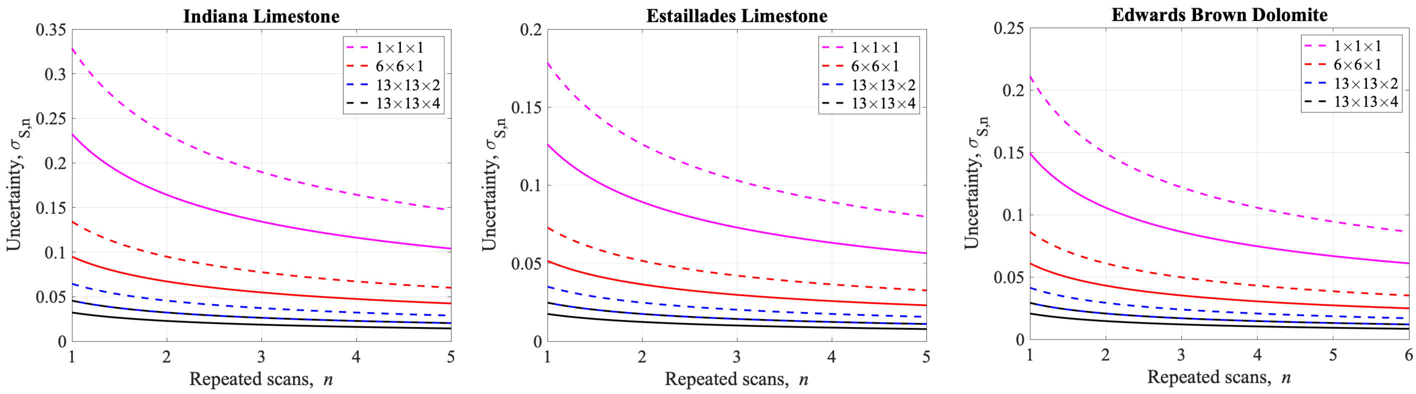

Figure S1. Uncertainty in the saturations as a function of the number of repeat scans for the three carbonate samples. Six repeat scans were available for the Edwards Brown dataset and five for the other two samples. The colours represent the uncertainty for specific coarsening schemes as indicated. The solid and dashed lines refer to the uncertainty at $S_w = 0.0$ and $S_w = 1.0$, respectively.

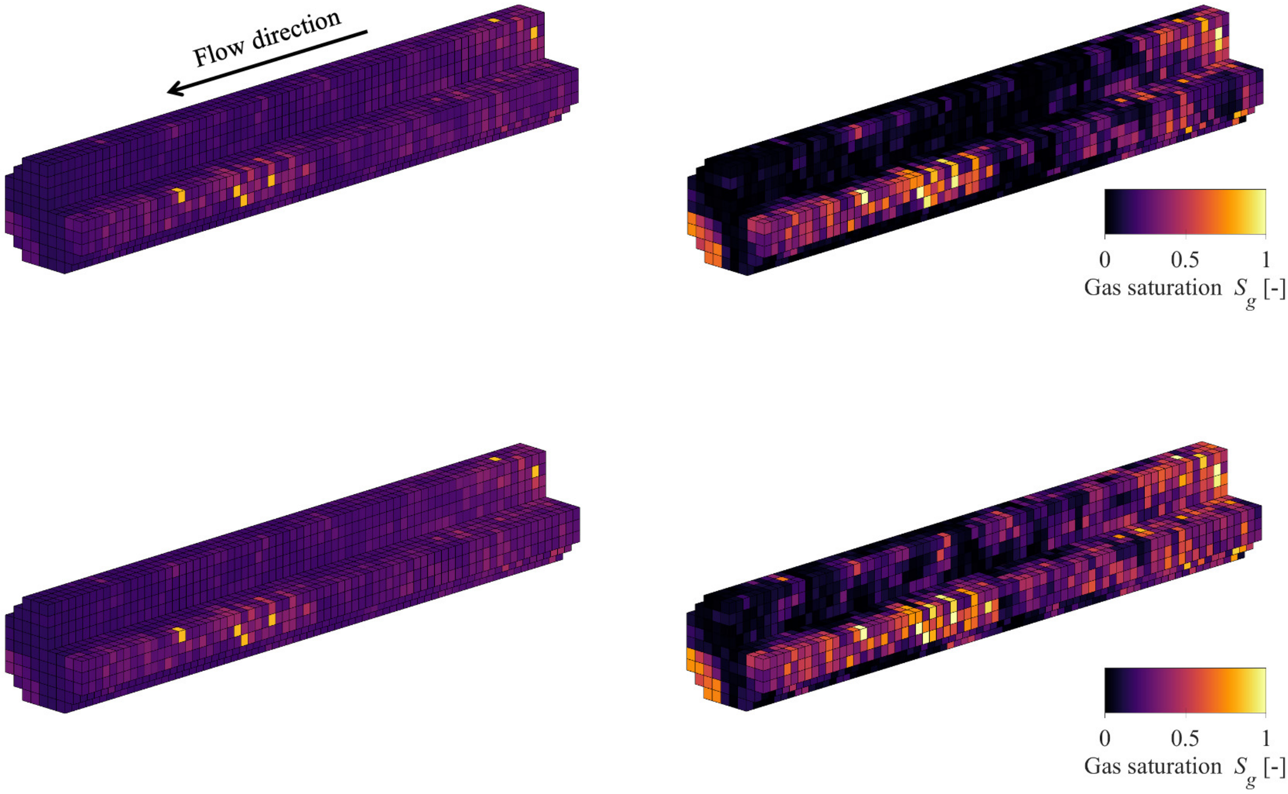

Figure S2. 3D saturation maps of the Indiana limestone for the simulation (left) and experiment (right) at two different fractional flows: $fN_2 = 0.612$ (top) and $fN_2 = 1.0$ (bottom). Digital core dimensions: $L = 0.144$m, r= 0.011m. The simulation displays a severe mismatch of the experimental voxel saturations.

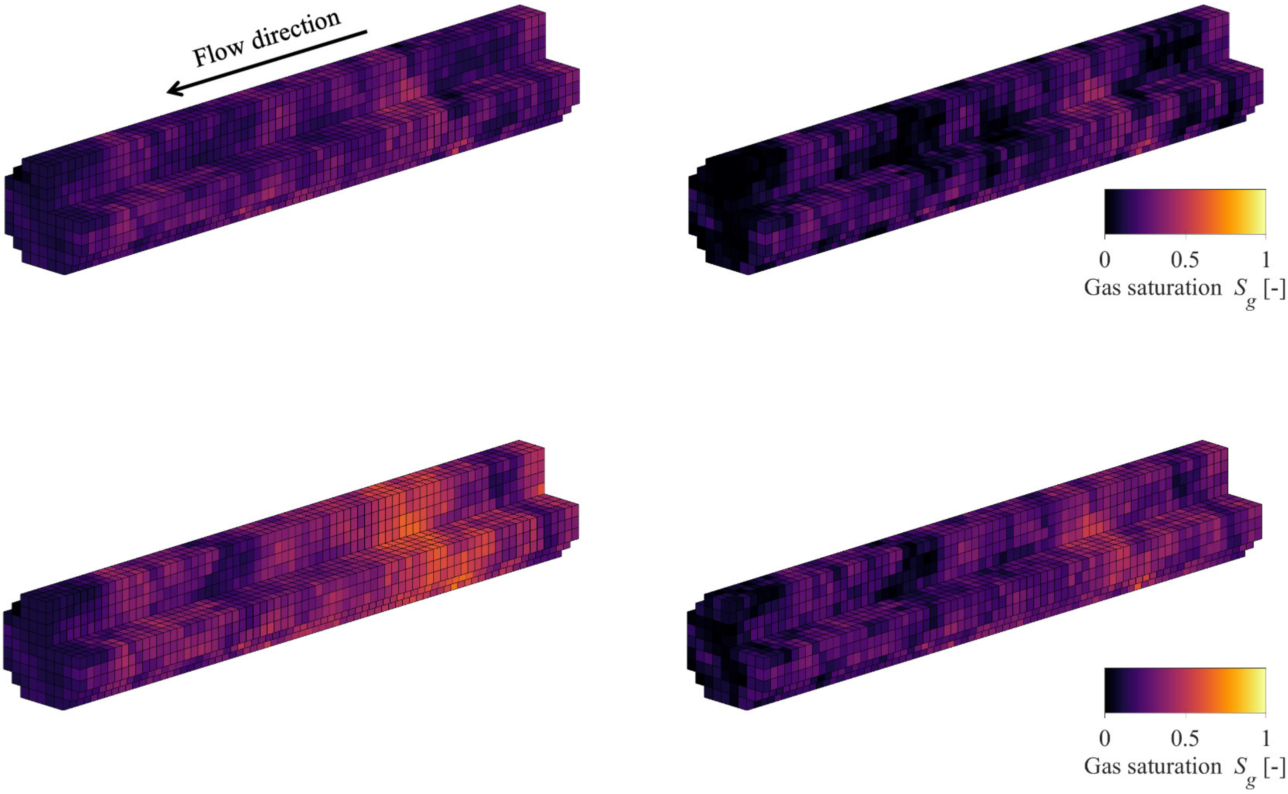

Figure S3. 3D saturation maps of the Estaillades limestone for the simulation (left) and experiment (right) at two different fractional flows: $fN_2 = 0.612$ (top) and $fN_2 = 1.0$ (bottom). Digital core dimensions: $L = 0.144$m, $r = 0.011$m. The Estaillades exhibits the closest match of the voxel saturations compared to the other two carbonates.

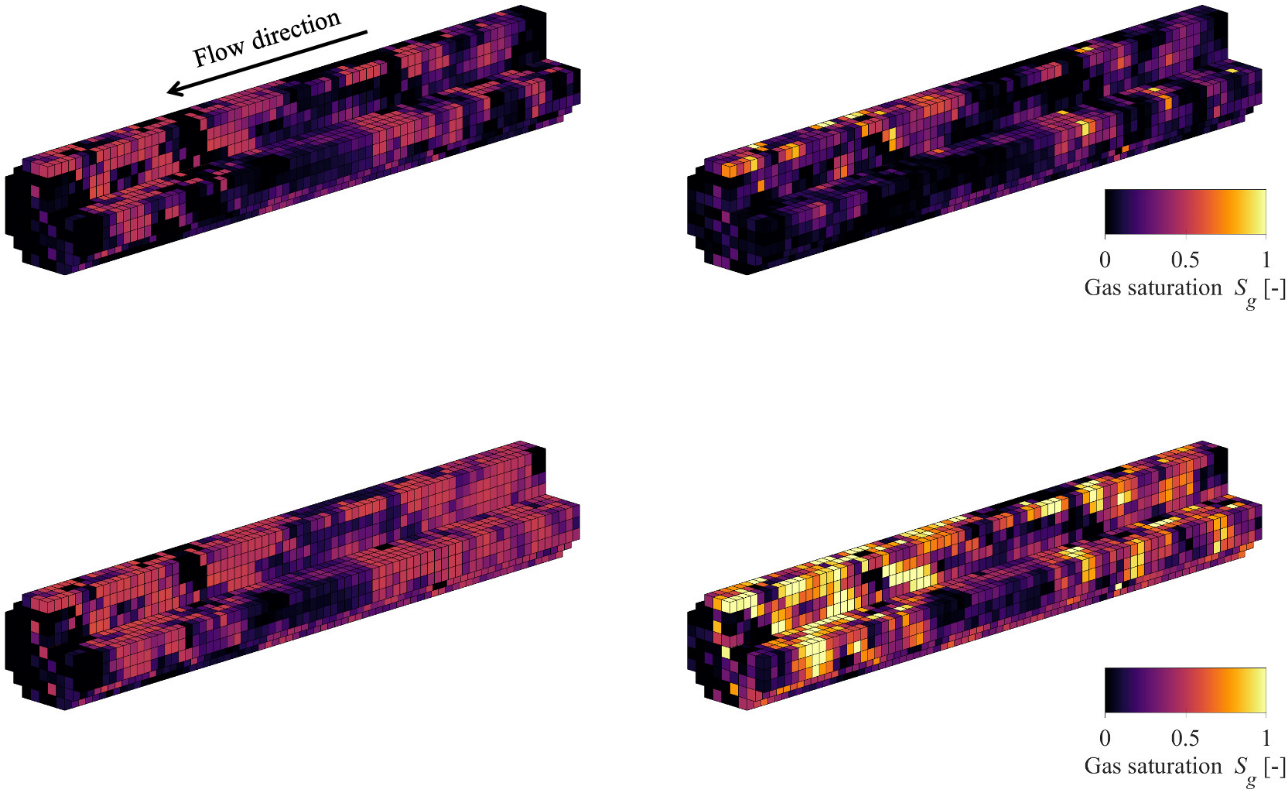

Figure S4. 3D saturation maps of the Edwards Brown dolomite for the simulation (left) and experiment (right) at two different fractional flows: $fN_2 = 0.612$ (top) and $fN_2 = 1.0$ (bottom). Digital core dimensions: $L = 0.144$m, $r=$ 0.011m. The general saturation distribution trend is well reproduced, but individual voxels display a significant mismatch.

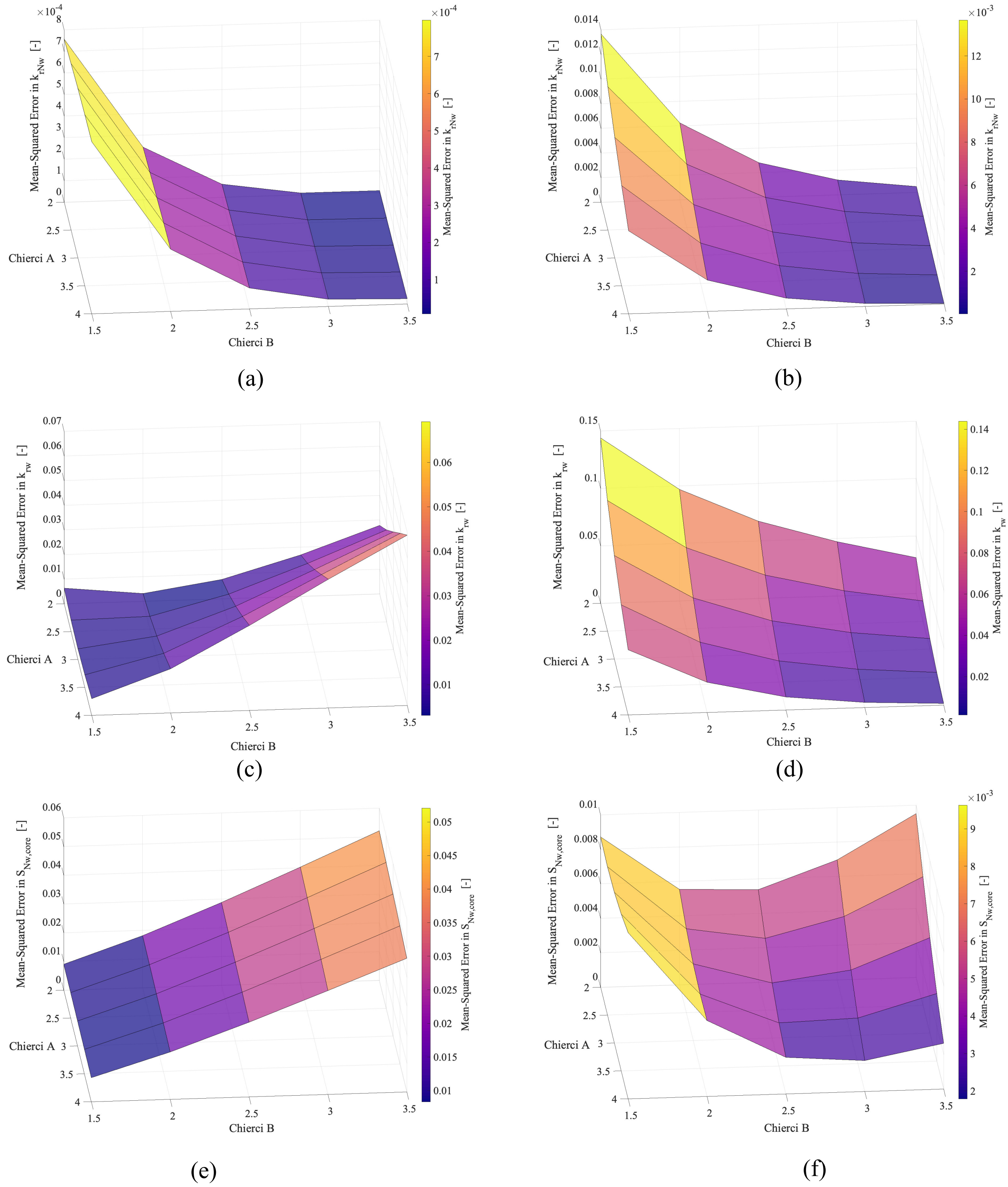

Figure S5. Mean-squared error between the simulation and experiment relative permeabilities and voxel saturations for the Indiana limestone. The errors are calculated using a range of A and B parameters as input. Figures (a), (c) and (e) are the errors for the low rate experiment and Figures (b), (d), (f) are the errors for the high rate experiment. The combination of Chierici parameters that minimises the errors significantly differs between both datasets.

Table S1. Relative Permeabilities for the Bentheimer sandstone at varying total flow rates. Data is displayed graphically in Figure 10 and was obtained from numerical simulations.

Capillary Number	**0.170**			**13.41**			**144.85**		
f_g	S_w	k_{rw}	k_{rg}	S_w	k_{rw}	k_{rg}	S_w	k_{rw}	k_{rg}
0.14	0.7210	0.0771	0.0005	0.6893	0.1620	0.0011	0.6612	0.1256	0.0008
0.4	0.6478	0.0489	0.0013	0.6294	0.1092	0.0029	0.6108	0.0867	0.0023
0.71	0.5853	0.0236	0.0024	0.5671	0.0664	0.0067	0.5621	0.0604	0.0061
0.86	0.5417	0.0097	0.0030	0.5143	0.0400	0.0125	0.5139	0.0412	0.0128
0.94	0.5208	0.0049	0.0033	0.4803	0.0273	0.0181	0.4787	0.0284	0.0189
0.99	0.4908	0.0006	0.0035	0.3934	0.0073	0.0409	0.3912	0.0076	0.0430

Table S2. Relative Permeabilities for the Bunter sandstone at varying total flow rates. Data is displayed graphically in Figure 10 and was obtained from numerical simulations.

Capillary Number	**0.130**			**13.31**			**72.24**		
f_g	S_w	k_{rw}	k_{rg}	S_w	k_{rw}	k_{rg}	S_w	k_{rw}	k_{rg}
0.1	0.7131	0.0464	0.0004	0.7781	0.3482	0.0031	0.7765	0.3487	0.0031
0.31	0.6677	0.0331	0.0012	0.6966	0.2129	0.0075	0.6970	0.2172	0.0077
0.63	0.6152	0.0176	0.0024	0.6126	0.1107	0.0149	0.6118	0.1191	0.0160
0.85	0.5677	0.0074	0.0033	0.5431	0.0527	0.0236	0.5365	0.0588	0.0263
0.98	0.5145	0.0013	0.0040	0.4539	0.0129	0.0396	0.4419	0.0145	0.0447
0.995	0.4899	0.0003	0.0042	0.3972	0.0034	0.0533	0.3836	0.0039	0.0612

Table S3. Relative Permeabilities for the Edwards Brown dolomite at varying total flow rates. Data is displayed graphically in Figure 10 and was obtained from numerical simulations.

Capillary Number	**0.007**			**0.129**			**5.904**		
f_g	S_w	k_{rw}	k_{rg}	S_w	k_{rw}	k_{rg}	S_w	k_{rw}	k_{rg}
0.024	1.0000	0.9601	0.0004	0.9232	0.3555	0.0002	0.9003	0.2609	0.0001
0.110	0.8823	0.0995	0.0002	0.8964	0.2299	0.0005	0.8652	0.2253	0.0005
0.200	0.8698	0.0856	0.0004	0.8839	0.1858	0.0009	0.8466	0.1987	0.0009
0.450	0.8505	0.0557	0.0008	0.8586	0.1239	0.0019	0.8386	0.1357	0.0020
0.740	0.8301	0.0259	0.0014	0.8260	0.0767	0.0040	0.8386	0.0642	0.0033
0.830	0.8233	0.0170	0.0015	0.8080	0.0623	0.0056	0.8219	0.0417	0.0037
0.960	0.7979	0.0041	0.0018	0.7529	0.0286	0.0126	0.7678	0.0116	0.0051
1.000	0.7940	0.0002	0.0019	0.6635	0.0035	0.0323	0.7021	0.0020	0.0183